Automotive Magneto-Rheological Dampers: Modelling and Parameter Identification using contrast-based Fruit Fly Optimisation

Kanarachos, S, Savitski, D, Lagaros, N & Fitzpatrick, M

Original citation & hyperlink:
Kanarachos, S, Savitski, D, Lagaros, N & Fitzpatrick, M 2017, 'Automotive Magneto-Rheological Dampers: Modelling and Parameter Identification using contrast-based Fruit Fly Optimisation' *Soft Computing*, vol (in press), pp. (in press)
https://dx.doi.org/10.1007/s00500-017-2757-6

DOI 10.1007/s00500-017-2757-6
ISSN 1432-7643
ESSN 1433-7479

Publisher: Springer

The final publication is available at Springer via http://dx.doi.org/10.1007/s00500-017-2757-6

Title:

Automotive Magneto-Rheological Dampers: Modelling and Parameter Identification using contrast-based Fruit Fly Optimisation

Abstract:

The present study discusses the mechanical behaviour and modelling of a prototype automotive magneto-rheological (*MR*) damper, which presents different viscous damping coefficients in jounce and rebound. The force generated by the *MR* damper is measured at different velocities and electrical currents, and a modified damper model is proposed to improve fitting of the experimental data. The model is calibrated by means of parameter identification and for this purpose a new swarm intelligence algorithm is proposed, that we call the *contrast-based Fruit Fly Optimisation Algorithm* (c-FOA). The performance of c-FOA is compared with that of Genetic Algorithms, Particle Swarm Optimisation, Differential Evolution and Artificial Bee Colony. The comparison is made on the basis of no *a-priori* knowledge of the damper model parameters range. The results confirm the good performance of c-FOA under parametric range uncertainty. A sensitivity analysis discusses c-FOA's performance with respect to its tuning parameters. Finally, a ride comfort simulation study quantifies the discrepancies in the results, for different identified damper model sets. The discrepancies underline the importance of accurately describing MR damper nonlinear behaviour, considering that virtual sign-off processes are increasingly gaining momentum in the automotive industry.

Stratis Kanarachos[a], Dzmitry Savitski[b], Nikos Lagaros[c] and Michael E. Fitzpatrick[a]

[a] stratis.kanarachos@coventry.ac.uk, ab6856@coventry.ac.uk, Faculty of Engineering, Environment and Computing, Coventry University, Priory Street, Coventry CV1 5FB, United Kingdom

[b] *dzmitry.savitski@tu-ilmenau.de, Automotive Engineering Group, Department of Mechanical Engineering, Technische Universität Ilmenau , Ehrenbergstr. 15, 98693 Ilmenau, Germany*

[c] *nlagaros@central.ntua.gr, School of Civil Engineering, National Technical University of Athens, 9 Heroon Polytechniou Str., Zografou Campus, Athens 157 80, Greece*

Corresponding author: *Stratis Kanarachos, stratis.kanarachos@coventry.ac.uk Tel: +44(0)2477657720, Engineering & Computing Building - EC 4-07, Faculty of Engineering, Environment and Computing, Coventry University, 3, Gulson Road, Coventry, CV1 2JH*

Keywords:
Model identification; Swarm intelligence; contrast-based fruit fly optimisation; automotive magneto-rheological dampers; ride comfort

1. INTRODUCTION

Magneto-rheological (MR) dampers find an increasing number of applications in civil, mechanical and automotive engineering [1-4]. Regarding the latter, Digital Design and Virtual Modelling have been identified as key elements for significantly reducing development costs and speeding up time to market [5]. Concurrently virtual testing and homologation is increasingly gaining momentum [6]. Pilot studies in the automotive industry show that costs can be reduced up to 5 times. Therefore, there is a need for tools that can model and accurately describe MR damper behaviour. Inaccurate MR damper modelling has been shown to lead to undesirable limit cycle behaviour, sub-optimal energy dissipation and insufficient control [7-8]. The inaccuracy is mainly due to MR dampers' highly nonlinear mechanical behaviour.

MR damper force is characterised by significant hysteresis [9-10] and delay, in the range of tens of milliseconds, owing to the inductance of the MR damper electro-magnetic circuit [11-12]. Damping characteristics can be continuously adapted by controlling the electrical current that passes through the electromagnet [13-15]. Furthermore, MR dampers can be mechanically designed to have different damping coefficient in jounce and rebound [16]. The latter is particularly important for automotive suspension control where the vehicle response is differentiated when hitting a pothole or a bump [17].

The models proposed for describing MR damper behaviour range from analytical first-principle to phenomenological ones. Cesmeci and Engin developed a theoretic flow model based on the Bingham plastic constitutive model and compared it to the modified Bouc-Wen damper model [18]. Guo *et al*. developed a more detailed version of the previous one by considering also the compressibility of MR fluid and air [19]. Both approaches aimed at developing an accurate physical model of damper hysteretic behaviour. On the other hand, both approaches do not take into account damper mass (inertia), while tests were conducted in a relatively small range of frequencies (less than 1 Hz). In [20] a lumped mass parameter model was developed as a response to accurately describing MR damper behaviour at different frequencies.

In [21] a hyperbolic tangent model was proposed for approximating the hysteretic behaviour, without the need to employ a set of differential equations. Recently Zhang *et al*. [22] proposed a sigmoid model for approximating the mechanical behaviour of an MR damper and compared its performance to the Bingham and Bouc-Wen models. Another alternative is to employ dynamic neural networks [22]. The disadvantage of using neural networks is that no insight is gained even when the model parameters are identified. In [23] the MR damper model is identified using the recursive lazy learning method. In lazy learning, each time a prediction is required for a specific query point, a set of local models is identified. The generalization ability of each model is assessed through a local cross-validation procedure. Finally, a prediction is obtained either by combining or selecting different local models on the basis of some statistic of their cross-validation errors. The optimal combination of models is achieved using a recursive formula.

As far as it concerns modelling in automotive applications, Silveira *et al*. idealised the damper as a single viscous damping element with different coefficients in jounce and rebound [24]. The hysteretic behaviour of the damper was not taken into account. Similar approaches were followed in [25] and [26] indicating current modelling practice in automotive engineering. In [27]-[29] the modified Bouc-Wen damper model was used for developing a semi-active suspension controller. The modified Bouc-Wen model enhances with a spring and a damper the original one to simulate more accurately the roll-off effect at small velocities. In that region the damper force drops more rapidly due to the fluid shear thinning effect.

Suppliers of MR dampers do not provide information relevant to the hysteretic or roll-off behaviour. To this end experimental tests are necessary for determining at greater accuracy the damper mechanical behaviour [30-32]. Engineers are left with the task of accurately fitting the experimental data by identifying the parameters of the models employed. For this purpose different optimisation were proposed in the past, including Particle Swarm Optimisation, Cascaded Evolutionary Algorithms, Recursive Lazy Learning, Adaptive Charged system, and Genetic Algorithms [33-39]. In [33] a radial basis function neural network (RBFNN) was employed to fit the data. The parameters of RBFNN were determined by applying sequentially a genetic (GA) and differential evolution (DE) algorithm. Differential evolution was employed as a means to improve the population generated by GA. The RBFNN used 13 neurons. As mentioned in [32] the choice of parameters in GA and DE is problem-dependent and

user experience was required. To this end different rules have been proposed in the literature but do not always provide the expected performance [34, 35]. The population size in DE was 100 and in GA 30. The crossover probability in DE was 0.6 and in GA 0.9. The mutation factor was 0.5 in both algorithms. In [36] the GA was implemented to identify the parameters of a non-symmetrical Bouc-Wen model. The non-symmetrical Bouc-Wen model is a variation of the original Bouc-Wen model for describing dampers with asymmetric hysteretic behaviour at near zero velocities. The GA used real-value random numbers to represent the chromosomes. The population size was 50. The selection operation was omitted. Crossover was realised by selecting randomly two chromosomes and generating a child using a linear blending function. Mutation is implemented by selecting randomly a chromosome and perturbing it using a Gaussian kernel. After crossover and mutation, 2% of the chromosomes were replaced by copies of the best chromosome. GA was terminated when the expectation of improving the identification error was below a threshold value. To identify the parameters of a modified Bouc-Wen model the Enriched Imperialist Competitive Algorithm (EICA) was used in [37]. The model comprises fourteen variables. The utilized test data covered velocities up to 30 mm/s. EICA is an agent-based optimisation algorithm. The agents of this algorithm are called "countries". There are two types of "countries"; those with the lower function value are selected to be the "imperialist" states and the remaining countries form the "colonies" of these imperialists. All the colonies of initial countries are divided among the imperialists based on their "influence". The influence of each "country" is inversely proportional to its cost. The Charged System Search was implemented in [38] to identify the parameters of the modified Bouc-Wen model. Charged system search uses Coulomb's and Newton's laws to describe the interactions taking place in a group of particles. A number of parameters need to be tuned for improving the trade-off between exploration and exploitation. The algorithm terminated after 200 iterations. The authors pointed out the importance of estimating correctly the range of parameters before optimisation starts. In the particular study this was achieved by a comprehensive parametric analysis, testing different search domains around the actual values of the parameters. Particle Swarm Optimisation (PSO) was utilised in [39] to identify the parameters of an algebraic MR damper model. The algebraic model included a hyperbolic tangent function to describe the hysteretic behaviour. In PSO the inertia term ω was 0.65 and parameters $\varphi_1 = \varphi_2 = 1$. The population comprised

50 members. The algorithm terminated when the probability of improving the objective function was below a threshold. The utilized test data were for velocities up to 50 mm/s.

The multitude of MR damper models indicates that model selection depends directly on the task. In dynamics and control the most popular one is the modified Bouc-Wen model [40]. This model employs a set of coupled differential equations to approximate the MR damper hysteretic behaviour. Consequently, simulation of damper force using Bouc-Wen requires longer time compared to algebraic damper models. In the parameter identification process the simulation routine may be called several thousand times and thus requires a long time to complete. A considerably longer parameter identification process may become a significant disadvantage for a commercial product or a tool used by practicing engineers. Furthermore, the modified Bouc-Wen model is not necessarily suitable for automotive MR dampers as it cannot approximate dampers with asymmetric viscous damping behaviour.

In this paper, the mechanical behaviour of a prototype automotive MR damper, with asymmetric viscous damping coefficient in jounce and rebound is presented. The MR damper was tested at a relevant range of velocities and currents and a modified algebraic damper model is proposed for improving the fitting of experimental data. An algebraic model is proposed as a means for minimising the time required for identification. For the parameter identification, the contrast-based Fruit Fly Optimisation Algorithm (c-FOA) is employed [41]. c-FOA is compared to the Genetic Algorithm, Differential Evolution, Particle Swarm Optimisation, Artificial Bee Colony and the original FOA. The comparison is performed under the assumption that the initial range of model parameters is unknown. The results show that the proposed contrast-based FOA is suitable for identifying the parameters of MR dampers. A sensitivity analysis was performed and the factors that influence c-FOA's performance are discussed. Finally, a ride comfort simulation study quantifies the discrepancies in the results, for different identified damper model sets. The discrepancies underline the importance of accurately describing MR damper nonlinear behaviour, considering that virtual sign-off processes are increasingly gaining momentum in the automotive industry.

The rest of the paper is structured as follows: in Section 2 the experimental data and the proposed asymmetric MR damper model are presented and discussed. In Section 3

c-FOA is explained. In Section 4 the performance of c-FOA is compared to Genetic Algorithm, Differential Evolution, Particle Swarm Optimisation, Artificial Bee Colony and the original FOA. In Section 5 an analysis is carried out for highlighting the tuning parameters of c-FOA and the computational burden reduction when processed in parallel. Finally, Section 6 gives conclusions, and future work is proposed.

2. ASYMMETRIC MR DAMPER MODEL

The prototype MR damper concerns a monotube damper configuration, asymmetric in terms of the magnitude of generated forces in both directions of the piston motion. The electromagnets are attached to the passages. As the MR fluid goes through the passage, and under the application of a magnetic field, the viscosity changes. The particles' size contained in the MR fluid ranges usually between 1μm and 7μm. As shown in Figure 1, in the absence of a magnetic field the particles take random positions; in the presence of a magnetic field they align. The stronger the magnetic field intensity B is, the greater the particles align [42]. The compressed length of the damper is 500 mm and the maximum stroke is 170 mm. The coil resistance is approximately 1.5 Ω.

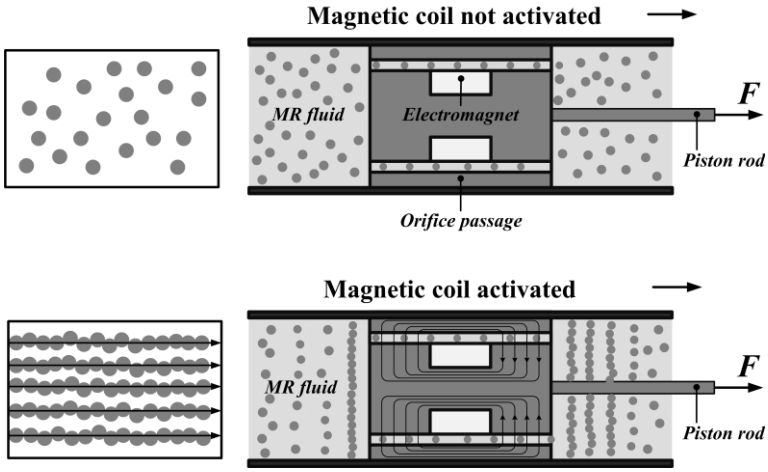

Figure 1 Alignment of iron particles contained in the MR fluid in the presence of a magnetic field

2.1 Experimental setup and MR damper force response

The experimental setup consists of a servo-hydraulic tensile test machine and an Electronic Control Unit that controls the current in the electromagnets, housed in the MR damper, Figure 2 [43]. The damper is driven by the servo-hydraulic tester and the

load cell measures the generated damping force. The tester is an Instron 8501, this is a 100 kN dynamic rated frame. The system is regulated by an Instron FastTrack 8800 control system. Force is measured using an Instron 10 kN load cell. Displacement is measured using an Instron 2601-093 linear variable displacement transducer (LVDT). To avoid extreme positions, the damper stroke was positioned at its centre before starting the test. Sampling rate was 250 Hz and 10 load cycles were collected in each test. The first and the last load cycle were omitted to avoid transient effects. The velocity is obtained from the derivative of displacement with respect to time. The maximum attainable velocity with the used testing machine is 0.15 m/s.

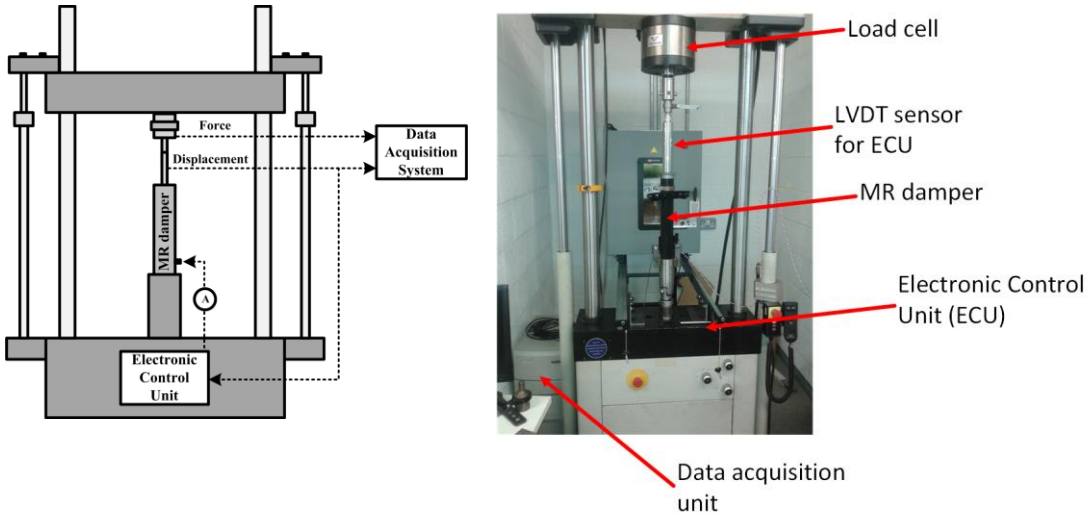

Figure 2. Experimental set up for testing the mechanical behaviour of the prototype MR damper.

The damper was tested for sinusoidal and triangle wave inputs $x(t)$ described by expressions (1) and (2) respectively:

$$x(t) = A \cdot \sin(2 \cdot \pi \cdot f \cdot t) \tag{1}$$

$$x(t) = A\frac{8}{\pi^2} \cdot \sum_{k=0}^{\infty} \frac{\sin(2 \cdot \pi \cdot (2 \cdot k + 1) \cdot f \cdot t)}{(2 \cdot k + 1)^2} \tag{2}$$

where A is the amplitude with $A \in [0, 0.05]$ m, f is the frequency of excitation with $f \in [0, 2]$ Hz and t is time. In the experiments the current I was varied from 0 to 2 A with the interval of 0.5 A.

Figure 3 illustrates the triangle wave input used for exciting the MR damper, where $A = 0.05$ m, $f = 1$ Hz.

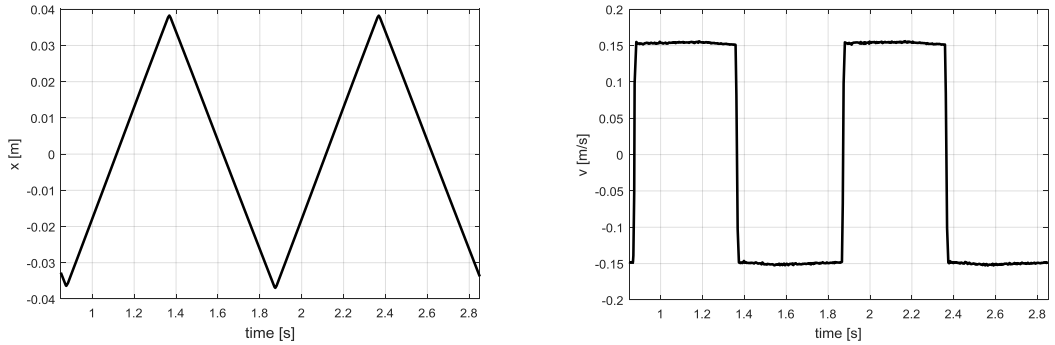

(a) (b)

Figure 3. Triangle wave input with $A = 0.05$ m, $f = 1$ Hz: a) Position versus time, b) Velocity versus time

Figure 4a shows a response of the damper force F_d to the triangle wave input with $I = 0$, and Figure 4b for the triangle wave input with $I = 0.5$ A. As observed, the hysteresis loop increased in size when the current was increased. The inclination of the force-velocity curve is different in jounce and rebound (the upper curve changes by 300 N while the lower curve changes approximately 450 N). The slope remained invariable when the current changed. Furthermore, damper force presents an offset at zero velocity. The offset is caused by pressurised gas in the accumulator in the damper.

Due to the offset and difference in inclination the damper behaves asymmetrically with respect to the positive and negative axis. For example, in Figure 4a the maximum positive force is approximately 200 N, while the maximum negative force is 630 N. In Figure 4b, the maximum positive force is 390 N, while the maximum negative force is 720 N.

For the model identification phase, the MR damper force response was tested for sinusoidal inputs with $A = 0.05$ m, $f = [0.5, 1, 1.5, 2\ ]$ Hz, and $I = [0.0, 0.5, 1.0, 1.5, 2.0]$ A . Table 1 lists the performed tests. Figure 5 illustrates the MR damper force response for sinusoidal input with $A = 0.05$ m, $f = 0.5$ Hz and $I = [0.0, 0.5, 1.0, 1.5, 2.0]$ A.

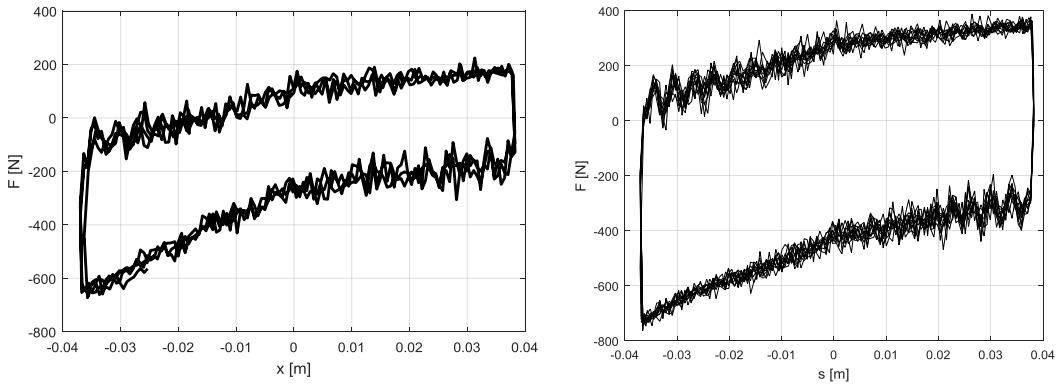

(a) (b)

Figure 4. MR damper force response for a triangle wave displacement with a) $A = 0.05$ m, $f = 1$ Hz, $I = 0$ b) $A = 0.05$ m, $f = 1$ Hz, $I = 0.5$ A.

Table 1. Loading conditions of the tests on the MR damper

	Frequencies f / Hz			
Electric current I / A	f=0.5	f =1	f =1.5	f =2
0	A=0.05 m	A=0.05 m	A=0.05 m	A=0.05 m
0.5	A=0.05 m	A=0.05 m	A=0.05 m	A=0.05 m
1	A=0.05 m	A=0.05 m	A=0.05 m	A=0.05m
1.5	A=0.05 m	A=0.05 m	A=0.05 m	A=0.05 m
2.0	A=0.05 m	A=0.05 m	A=0.05 m	A=0.05 m

The MR damper force response is again asymmetric. The maximum positive forces take lower values compared to the maximum negative forces. This is due to the offset and slightly asymmetric hysteretic behaviour. An additional reason for the asymmetry is the different slope of the MR damper force response for absolute velocities greater than approximately 0.07 m/s. A careful observation reveals that the damper force response for negative velocities is closer to the horizontal compared to the one achieved for positive velocities. This is an indication of the different viscous damping coefficient for jounce and rebound.

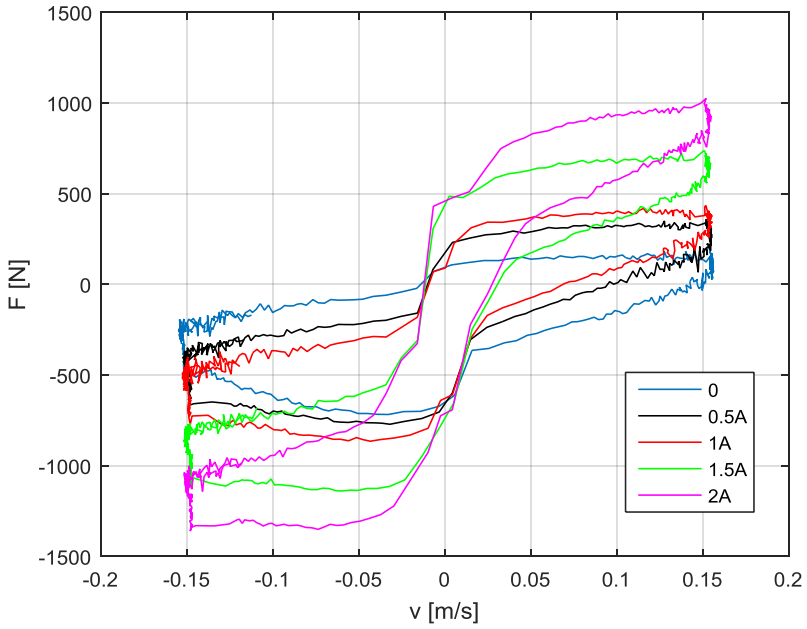

Figure 5. Experimental data used in the model identification phase: Force response for sinusoidal input with $A = 0.05$ m, $f = 0.5$ Hz and $I = [0.0, 0.5, 1.0, 1.5, 2.0]$ A.

2.2 Proposed asymmetric MR damper model

The proposed asymmetric model is developed on the basis of [12]. A detailed analysis of this model is provided in [39], where it was shown that it can accurately describe the hysteretic and roll-off behaviour of MR dampers. In order to minimize the time required for simulation and parameter identification an algebraic model was selected instead of one that is described by differential equations. Potentially, other algebraic models could serve the same purpose.

The damper force F_d is expressed by four elements:

$$F_d = m \cdot \ddot{u} + C_c \cdot \dot{u} + K_k \cdot u + F_h + F_0 \tag{3}$$

where F_d and u are the damping force and displacement of the MR damper respectively; C_c is the variable damping coefficient; K_k is the variable stiffness coefficient; m is the equivalent mass that represents the *MR* damper piston rod inertial effect and F_0 is the initial or preload force. The hysteretic force F_h is expressed as:

$$F_h = F_y \cdot tanh(y) \tag{4}$$

and

$$y = \beta \cdot \left(\dot{u} + \lambda \cdot sgn(u)\right) \tag{5}$$

where F_y is the damping force related to the magnetic field and β, λ are shape factors that determine the degree of smoothness of the hysteretic curves.

Parameters C_c, F_y and K_k are a function of current I [12]:

$$C_c(I) = C_{ca} + C_{cb} \cdot I \tag{6}$$

$$F_y(I) = F_{ya} + F_{yb} \cdot I \tag{7}$$

$$K_k(I) = K_{ka} + K_{kb} \cdot I \tag{8}$$

Parameters C_c, F_y and K_k depend linearly on current I because the prototype MR damper saturates at currents much larger other known configurations of a damper. For reliability purposes, it is not intended to use the *MR* damper at its limits.

The time response of the current I under a commanded input I_{cmd} is described by a first order model [12]:

$$\dot{I} = -\eta \cdot (I - I_{cmd}) \tag{9}$$

where η is a constant.

To account for the asymmetric damping forces the model described by Eqs (4)-(9) is refined as follows:

$$F_d = m \cdot \ddot{u} + C_c^* \cdot \dot{u} + K_k \cdot u + F_h + F_0 \tag{10}$$

with

$$C_c^* = \begin{cases} C_{ca}^+ + C_{cb}^+ \cdot I, if\ \dot{u} \geq 0 \\ C_{ca}^- + C_{cb}^- \cdot I, if\ \dot{u} < 0 \end{cases} \tag{11}$$

As observed for $\dot{u} = 0$ the damping force term F_c will be $F_c = C_c^* \cdot \dot{u} = 0$ and therefore zero order continuity C^0 is preserved.

In conclusion, the following thirteen parameters are used to describe the MR damper: $\mathbf{s} = [m, F_0, \beta, \lambda, F_{ya} F_{yb}, C_{ca}^+, C_{ca}^-, C_{cb}^+, C_{cb}^-, K_{ka}, K_{kb}, \eta]$.

3. CONTRAST BASED FRUIT FLY OPTIMISATION

3.1 Objective function formulation

The offset and noise in the experimental data were not removed, although this was possible by balancing and low-pass filtering, respectively. The reason for this was our aim to assess the optimisation algorithm's performance in the presence of epistemic uncertainty.

In order to obtain the parameters **s** that best fit the experimental data, the model identification problem is formulated as [44]:

Find optimal $\mathbf{s}^*$, $\mathbf{s} = [s_1, s_2, \dots, s_m]$

that minimises

$$f(\mathbf{s}) = \sum_{i=1}^{n} \left(F_{di,exp} \cdot v_i - F_{di} \cdot v_i\right)^2 \tag{12}$$

where vector **s** is the design vector, n is the number of sample data, $F_{di,exp}$ is the i^{th} measured damper force value, F_{di} is the i^{th} model predicted damper force value.

3.2 The Contrast-based Fruit Fly Optimisation Algorithm (c-FOA)

Pan presented for the first time the Fruit Fly Optimisation Algorithm (FOA), and since then different versions were developed, improving the efficiency and robustness of the initial FOA [45-48]. In this paper, the contrast-based Fruit Fly Optimisation Algorithm (c-FOA), an extension of original *FOA*, is presented. It is based on a recent biological study where it was discovered that fruit flies, when searching for food, are stimulated not only by smell but also by visually-contrasting objects [49]. Additionally, it was found that fruit fly cruising speed is dependent on the stimulation level: i.e., when the scent is strong fruit flies surge while when it is weak they cast. In this study, the fruit fly behaviour is accordingly idealised, modelled and further developed to address the parameter identification problem of an *MR* damper.

The basic steps of c-FOA are summarised by the pseudo-code shown in Figure 6, while a flowchart is provided in Figure 7.

Contrast-based Fruit Fly Optimisation Algorithm (c-FOA)

1: **begin**
2: Select initial design vector $\boldsymbol{s}_0$, *m is the number of* design variables
3: Generate initial fruit fly swarm $\boldsymbol{si}$, $i = 1,2, \dots, N$ in the vicinity of $\mathbf{s}_0$ using a uniform discrete distribution $[1, N_{res}]$
4: Calculate smell concentration (objective function) $\mathrm{Sm_i}$ at $\mathbf{s_i}$, $\mathrm{Sm_i} = \mathrm{f}(\mathbf{s_i})$
5: Rank the fruit flies' performance and find the best performing one $\mathrm{Sm}^* = \mathrm{f}(\mathbf{s}^*) = \min(\mathrm{Sm_i})$
6: If $\mathrm{Sm}^* < \mathrm{Sm}_0$ then $\boldsymbol{s}_0 = \mathbf{s}_\mathrm{i}^*$
7: **while** $(k < K)$
8: Increment k
9: Reposition the fruit fly swarm $\boldsymbol{s}_i[k]$, near $\boldsymbol{s}_0[k]$ using uniform discrete distribution $[1, N_{res}]$
10: Calculate smell concentration $\mathrm{Sm_i}[k] = f(\boldsymbol{s}_i[k])$
11: Rank the fruit flies and find the best:
12: $\mathrm{Sm}^*[\mathrm{k}] = \mathrm{f}(\mathbf{s}^*[\mathrm{k}]) = \min(\mathrm{Sm_i}[\mathrm{k}])$
13: If $\mathrm{Sm}^*[\mathrm{k}] < \mathrm{Sm}_0[\mathrm{k}]$ then $\boldsymbol{s}_0[k+1] = \boldsymbol{s}^*[k]$
14: Increment response time $t[k] = t[k-1] + 1$
15: **if** $(t[k] > delay\ time)$
16: **if** $(\mathrm{Sm}^*[\mathrm{k}] < \mathrm{Sm}_0[\mathrm{k} - \kappa])$
17: reduce the search radius $\mathrm{M}[\mathrm{k}+1] = \mathrm{c} \cdot \mathrm{M}[\mathrm{k}]$ (surging phase)
18: **else if** $(\mathrm{Sm}^*[\mathrm{k}] = \mathrm{Sm}_0[\mathrm{k} - \kappa])$
19: the worst performing candidate, $\mathbf{s}^{\because}[\mathrm{k}]$, $\mathrm{Sm}^{\because}[\mathrm{k}] = \mathrm{f}(\mathbf{s}^{\because}[\mathrm{k}]) = \max(\mathrm{Sm_i}[\mathrm{k}])$, becomes the new attraction point $\boldsymbol{s}_0[[k+1] = \boldsymbol{s}^{\because}[k]$ (contrast based vision phase)
20: **else if** $(\mathrm{Sm}^*[\mathrm{k}] > \mathrm{Sm}_0[\mathrm{k} - \kappa])$
21: return to the previous best, $\boldsymbol{s}_0[[k+1] = \boldsymbol{s}_0[[k-\kappa]$ (casting phase and memory function)
22: **end if**
23: Initialise response time $t[k] = 0$
24: **end if**
25: **end while**
26: *Post process results and visualisation*
27: **end**

Figure 6. Pseudo-code of the Contrast-based Fruit Optimisation Algorithm (c-FOA).

3.3 Swarm localisation, normalisation and termination

A coordinate system is defined and the position of a fruit fly with coordinates (X_0, Y_0) is defined. The remaining N–1 fruit flies are located, randomly, in the vicinity of (X_0, Y_0) according to Eq. (13).

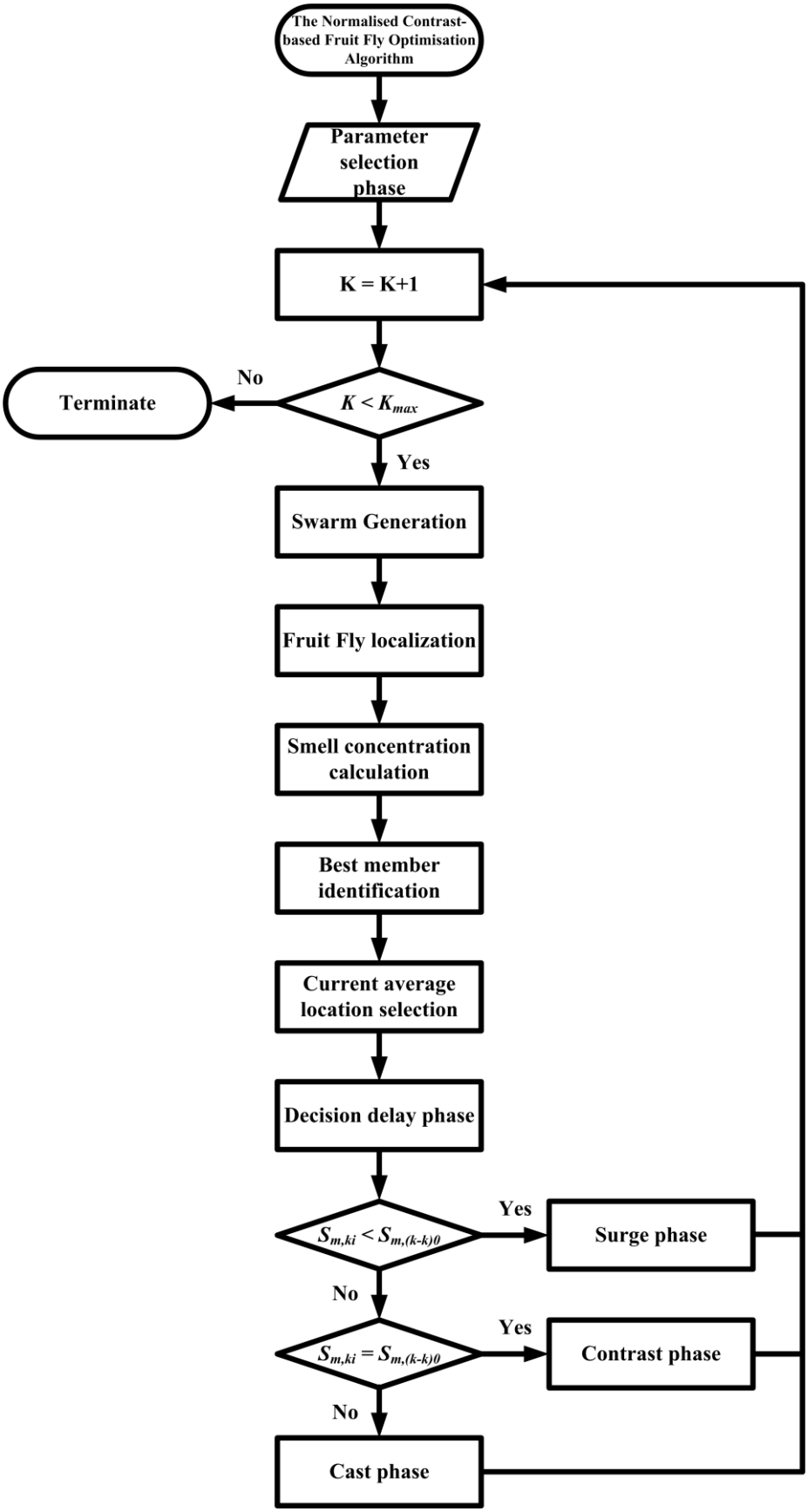

Figure 7. Flowchart of proposed *c-FOA* algorithm.

$$X_{ij}[k] = X_{0j}[k] \cdot \left(1 + M \cdot (2 \cdot rand_{N_{res}} - 1\right), j=1,2,\ldots,m \text{ and } i=1,\ldots,N$$
$$Y_{ij}[k] = Y_{0j}[k] \cdot \left(1 + M \cdot (2 \cdot rand_{N_{res}} - 1\right), j=1,2,\ldots,m \text{ and } i=1,\ldots,N \quad (13)$$

where k=1,2,…, K is the iteration number, m is the number of optimisation variables, N is the size of the swarm and $rand_{N_{res}}$ is a random number from a uniform discrete distribution defined in the interval [1, N_{res}]. The use of a discrete distribution is not observed in nature, but is a feature introduced to improve the algorithm's performance in multi-parameter problems. M is a scaling parameter that defines how coarse or fine the search strategy is.

To each fruit fly a smell concentration DI_{ij} is assigned based on how close each fruit fly parameter ($X_{ij}[k]$, $Y_{ij}[k]$) is to the origin of the coordinate system:

$$D_{ij}[k] = \sqrt{X_{ij}^2[k] + Y_{ij}^2[k]} \quad (14)$$

$$DI_{ij}[k] = sign(X_{ij}[k]) \cdot sign(Y_{ij}[k]) \cdot \frac{1}{D_{ij}[k]} \quad (15)$$

Each fruit fly is assigned a "smell concentration" $Sm_i[k]$ at $\mathbf{s_i}[k]$ determined by the objective function value $Sm_i[k] = f(\mathbf{s}_\mathbf{i}[k])$. A small objective function value corresponds to a position with high smell concentration, a position that is closer to the "food" source or the optimized value.

The fruit flies are ranked on the basis of their smell concentration, and the fruit fly $\mathbf{s}_i^*[k]$ that achieves the highest smell concentration $Sm_i^*[k]$ at position ($X_i^*[k]$, $Y_i^*[k]$) is identified. In case the smell concentration $Sm_i^*[k]$ is better than that of the current point of attraction $S_0[k]$, then $Sm_i^*[k]$ becomes the new point of attraction.

$$\boldsymbol{if\ Sm_i^* < S_{m,k0}}$$
$$then\ X_0[k] = X_i^*[k]\ and\ Y_0[k] = Y_i^*[k] \quad (16)$$

The algorithm terminates when the maximum number K of iterations is reached.

3.4 Response delay, cast, surge and visual contrast phases

Fruit flies do not respond immediately owing to sensory-motor delays when the stimulation changes. As presented in [49], the delay is constant and independent of other parameters. This delay is idealised and modelled in the *c-FOA* algorithm as follows.

In the case the best objective function value improves over the last κ iterations, where κ represents the delay, the swarm enters the "surge" phase, during which the fruit flies move towards the attraction point $\mathbf{s}_0[k]$ at greater speeds:

$$if\ (S_{mki} < S_{m(k-\kappa)0}) \qquad \boldsymbol{M_{k+1} = c \cdot M_k} \tag{17}$$

The requirement for the completion of κ iterations before a decision is made is inspired by fruit flies' food search behaviour. Fruit flies also present a delay in decision-making, most probably for compensating the chaotic movement of smell outdoors [49].

In case the best objective function value does not change over the last κ iterations the swarm enters the "visual contrast" phase, during which the fruit flies are attracted by the point $\mathbf{s}_i^{\cdot\cdot}[k]$ that achieves the lowest smell concentration $\max(Sm_i[k]) = Sm_i^{\cdot\cdot}[k]$:

$$if\ (Sm_i[k] = Sm_0[k-\kappa] \qquad X_0[k] = X_i^{\cdot\cdot}[k]\ and\ Y_0[k] = Y_i^{\cdot\cdot}[k] \tag{18}$$

where k is the current iteration.

$$if\ (Sm_i[k] > Sm_0[k-\kappa]) \qquad X_0[k] = X_0[k-\kappa]\ and\ Y_0[k] = Y_0[k-\kappa] \tag{19}$$

This resembles the memory function of fruit flies [50].

4. DAMPER MODEL IDENTIFICATION

The model identification problem was solved using the Genetic Algorithm, Differential Evolution, Particle Swarm Optimisation, Artificial Bee Colony, original *FOA* and *c-FOA*. All algorithms were implemented in MATLAB, version 16a. The

algorithms were terminated after 4000, 8000 and 16000 function evaluations (fun_evals). 30 independent repetitions were conducted to analyse statistically the performance of each algorithm. The reason for this is the stochastic behaviour of the optimisation algorithms. The only optimisation parameter varied was the population size. The rest of the optimisation parameters were not varied. However recommended/standard values were used [51-55]. It was assumed that there is no *a priori* knowledge of the damper model parameters range. Therefore, the design space was considered unbounded.

The Genetic Algorithm (GA) version utilised in this study is the one provided in the Global Optimisation Toolbox, MATLAB. Three different population sizes were tested, comprising 50, 100 and 150 members. A uniform distribution generates randomly the members using the floating-point representation. To each member objective function values are assigned and sorted according to it. 80% of the new generation is created by crossover and 5% progresses from the old generation. A stochastic uniform algorithm is used for the parent selection. The crossover operator uses a weighted average of the parents for creating the new generation. Mutation is used to create to remaining members. In mutation, the new directions are randomly picked up. GA terminated when the maximum number of function evaluations generations is reached, unless it stalled. This happens when for over 200 generations the objective function does not change significantly.

The Differential Evolution (DE) version employed in this study is from [56] and is the standard DE augmented with dither. This is a more robust version compared to the standard one. The population comprised 50, 100 and 150 members. The mutation operator was $F = 0.85$. The crossover probability in the crossover operator was $Cr = 1$. A uniform distribution created the individuals. DE internally treats all variables as floating-point values regardless of their type. DE terminated when the maximum number of function evaluations was reached.

The Particle Swarm Optimisation (PSO) version employed is the one available in MATLAB, version 16a. The initial swarm was generated randomly. The algorithm chooses the new member positions based on:

$$\boldsymbol{v_{i+1}} = \boldsymbol{\omega} \cdot \boldsymbol{v_i} + \boldsymbol{\varphi_1} \cdot \boldsymbol{\beta_1} \cdot (\boldsymbol{p_i} - \boldsymbol{x_i}) + \boldsymbol{\varphi_2} \cdot \boldsymbol{\beta_2} \cdot (\boldsymbol{p_g} - \boldsymbol{x_i})$$
$$x_{i+1} = x_i + v_{i+1} \tag{20}$$

The inertia term $\omega\epsilon[0.1,1.1]$ is calculated in relation to the number of stalls c:

$$if\ c < 2,\ \ \omega_{i+1} = 2 \cdot \omega_i$$
$$elseif\ \ c > 5,\ \ \omega_{i+1} = \frac{\omega_i}{2} \tag{21}$$

In the case the objective function does not improve between two consecutive iterations, the neighbourhood size Nh is changed according to:

$$Nh_{i+1} = \min(Nh_i + Nh_{min}, N) \tag{22}$$

where $N = 50, 100$ and 150 is the total number of particles and $Nh_{min} = 0.25$ is the minimum number of particles. The parameters φ_1 and φ_2 were set as $\varphi_1 = \varphi_2 = 1.49$. PSO terminated when the maximum number of function evaluations was reached.

The Artificial Bee Colony algorithm (I-ABC) version was used in this comparison [57]. The total number of employed bees was $N = 50, 100$ and 150. The greedy selection mechanism was employed as the selection operator. The upper bound of the acceleration coefficient was $\Phi_2 = 1$. I-ABC terminated when the maximum number of function evaluations was reached.

The original Fruit Fly Optimisation Algorithm (FOA) employed in this study is detailed in [58]. The population size was set equal to $N = 50, 100$ and 150 members. For *c-FOA* the following parameters are selected: $N = 50, \kappa = 5, M = 0.95, N_{res} = 100$ and $c = 0.9$. FOA terminated when the maximum number of function evaluations was reached.

4.1 Data fit performance

In Table 2 the results of the statistical analysis for the 30 repetitions are listed. The results correspond to the set of optimisation parameters that achieved the best average value. A detailed analysis of the algorithms performance is provided in Appendix A, Tables 10-14. The mean value of the optimized values is denoted MV, the standard deviation SD and the best optimized value BV. As observed PSO and c-FOA achieve the best performance compared to the rest algorithms. PSO achieves a slightly better objective function value, while c-FOA reaches a slightly better average value. The result of the Kruskal-Wallis test is shown in Figure 8. The probability for the null hypothesis is p=0.03.

The authors also investigated how well c-FOA fits the data when a symmetric model is employed, where $C_{ca}^{-} = C_{ca}^{+},\ C_{cb}^{-} = C_{cb}^{+}$ (refer to Eq. 11). As observed, in Table 3, the asymmetric model achieves a better fit compared to the symmetric one. Therefore, it is possible to conclude that an asymmetric model is more suitable than a symmetric one, at least for the proposed type of MR damper model.

Table 2. Statistical analysis of the optimisation results obtained by applying, 30 independent times, the Genetic Algorithm, Differential Evolution, Particle Swarm Optimisation, Artificial Bee Colony, standard FOA and c-FOA. BV: Best value, MV: Mean value, SD: Standard deviation

			Objective function value $f(\mathbf{s})$		
	N	fun_{evals}	*BV*	*MV*	*SD*
Genetic Algorithm	100	16000	$4.14 \cdot 10^{7}$	$4.67 \cdot 10^{7}$	$3.11 \cdot 10^{6}$
Differential Evolution	50	16000	$3.76 \cdot 10^{8}$	$9.31 \cdot 10^{8}$	$4.66 \cdot 10^{8}$
Particle Swarm Optimisation	100	16000	$3.39 \cdot 10^{7}$	$5.44 \cdot 10^{7}$	$1.40 \cdot 10^{7}$
Artificial Bee Colony	50	16000	$2.96 \cdot 10^{9}$	$1.14 \cdot 10^{10}$	$6.39 \cdot 10^{9}$
FOA	50	16000	$2.00 \cdot 10^{17}$	$2.00 \cdot 10^{17}$	$3.40 \cdot 10^{10}$
c-FOA	50	16000	$3.40 \cdot 10^{7}$	$4.53 \cdot 10^{7}$	$1.44 \cdot 10^{7}$

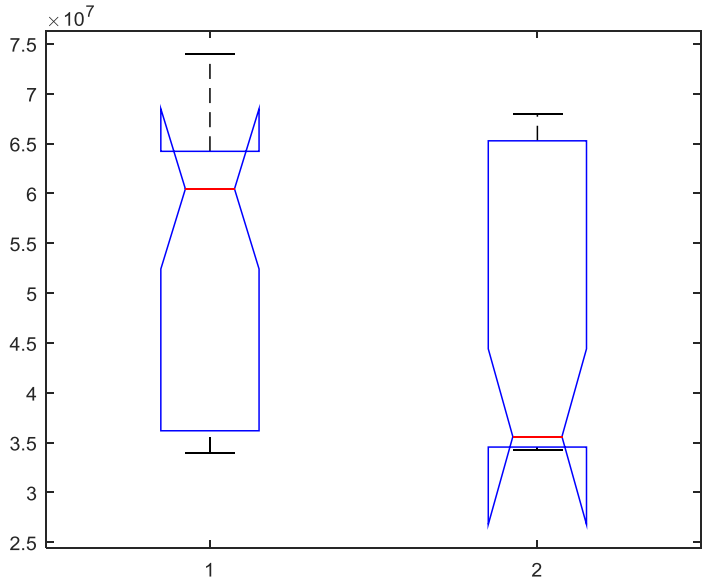

Figure 8. Kruskal-Wallis test output and box plots for the optimisation results obtained from PSO ("1") and c-FOA ("2")

Table 3. Statistical analysis of the optimisation results obtained by applying, 30 independent times, c-FOA using an asymmetric and a symmetric model. BV: Best value, MV: Mean value, SD: Standard deviation

c-FOA			Objective function value $f(\mathbf{s})$		
	N	fun_{evals}	*BV*	*MV*	*SD*
Asymmetric model $C_{ca}^{-} \neq C_{ca}^{+}$ $C_{cb}^{-} \neq C_{cb}^{+}$	50	16000	$3.40 \cdot 10^7$	$4.53 \cdot 10^7$	$1.44 \cdot 10^7$
Symmetric model $C_{ca}^{-} = C_{ca}^{+}$ $C_{cb}^{-} = C_{cb}^{+}$	50	16000	$6.39 \cdot 10^7$	$7.73 \cdot 10^7$	$1.70 \cdot 10^7$

The model parameters that produced the best fit using c-FOA, are listed in Table 4.

An example of c-FOA convergence rate is illustrated in Figure 9.

Table 4. Optimised model parameter values using *c-FOA*

Parameter No.	*c-FOA* $f(\mathbf{s}) = 3.40 \cdot 10^7$	
1	m	3.83
2	F_0	–270.00
3	β	144.00
4	λ	1.41

5	F_{ya}	5.56
6	F_{yb}	238.00
7	C_{ca}^{+}	2278.00
8	C_{ca}^{-}	98.00
9	C_{cb}^{+}	46.00
10	C_{cb}^{-}	178.00
11	K_{ka}	3.70
12	K_{kb}	1.07
13	η	25.00

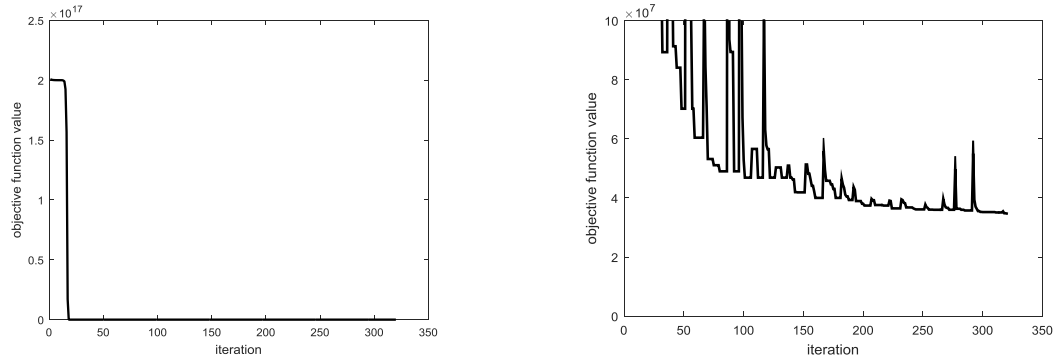

(a) (b)

Figure 9. Convergence rate example with *c-FOA* (a) Overall view (b) Detailed view

The model-based and measured damper forces versus speed for a sinusoidal input with $A = 0.05$ m, $f = 0.5$ Hz are illustrated in Figure 10. Figure 10a corresponds to an input with $I = 0$, Figure 10b to $I = 0.5$ A, Figure 10c to $I = 1.5$ A and Figure 10d to $I = 2$ A. As observed there is a good match between the two curves, however the match is not identical. It is observed that only for $I = 2$ A at low speed the damper force curve suddenly changes the slope. This behaviour is not observed in the rest cases. The corresponding damper force-displacement diagrams are provided in Figure 11.

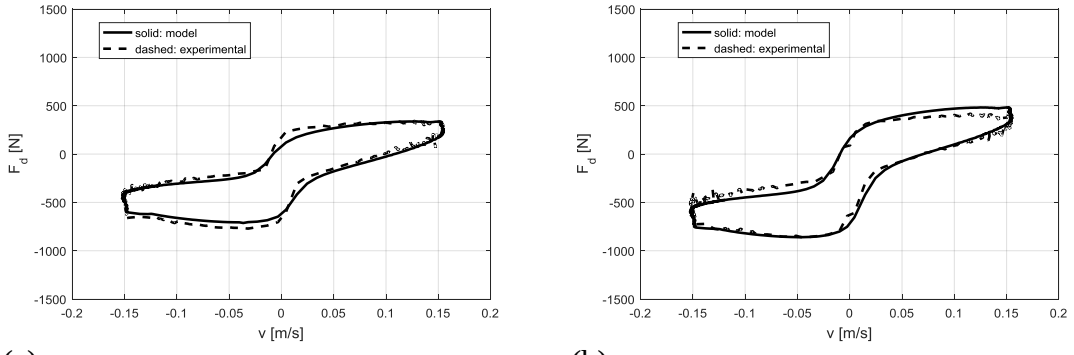

(a) (b)

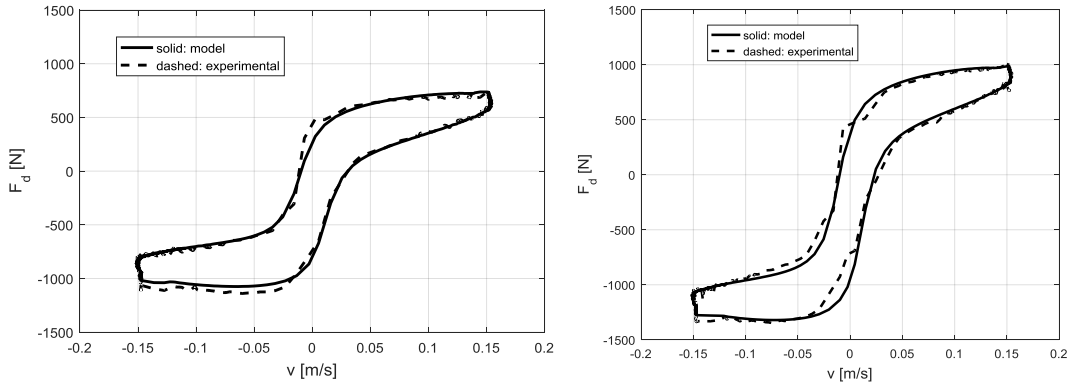

Figure 10. Damper force-versus speed diagrams. Comparison between experimental data and simulation for $A = 0.05$ m, $f = 0.5$ Hz a) $I = 0.5$ A. b) $I = 1$ A, c) $I = 1.5$ A and d) $I = 2$ A.

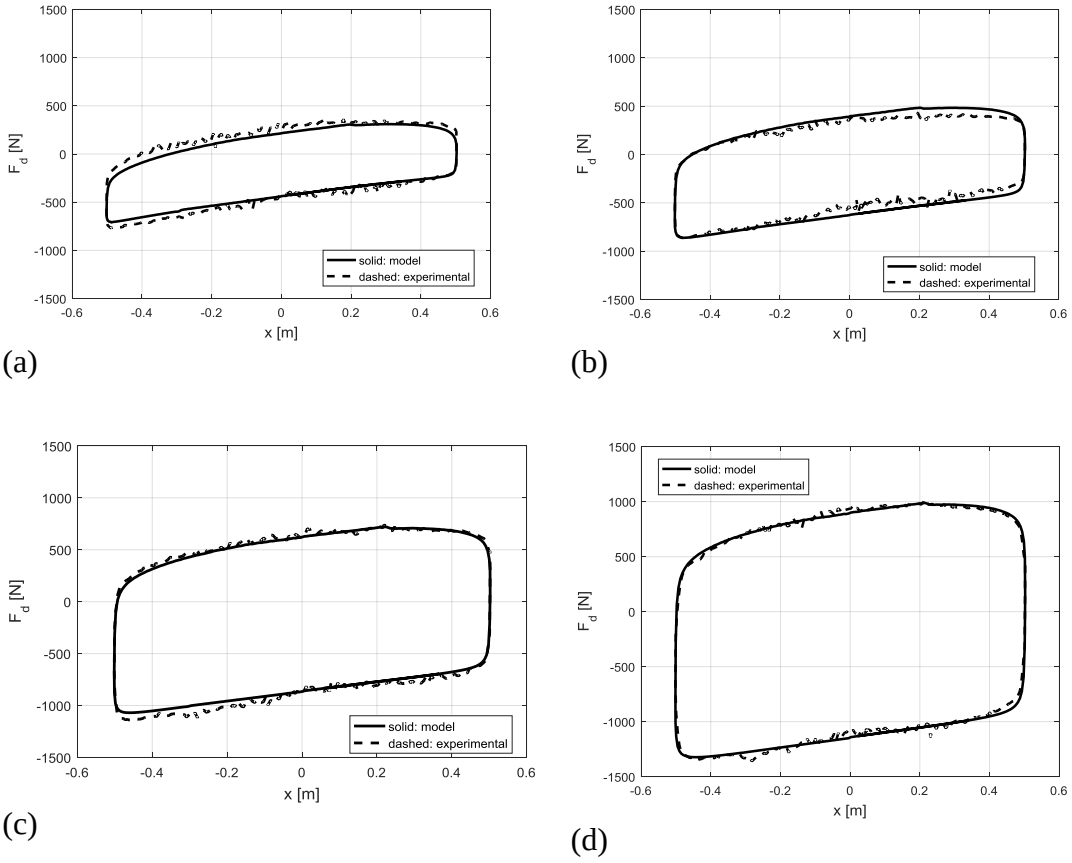

Figure 11. Damper force-versus displacement diagrams. Comparison between experimental data and simulation for $A = 0.05$ m, $f = 0.5$ Hz a) $I = 0.5$ A. b) $I = 1$ A, c) $I = 1.5$ A and d) $I = 2$ A.

4.2 Damper model identification and ride comfort CAE analysis

A proper parameterization of the *MR* dampers plays an important role in ride comfort Computer Aided Engineering (CAE) analysis [59]. The importance of virtual testing and virtual sign-off gains are increasing momentum in the automotive industry. In several cases it was demonstrated that virtual sign-off can reduce costs up to 5 times.

A ride comfort scenario was investigated for three different model parameter fits. The model parameters correspond to the best solution identified by c-FOA, GA and PSO. The corresponding model parameters are listed in Table 5.

For the simulation a sport utility vehicle (SUV) vehicle of total mass 1963 kg is considered. Compliance and kinematics of the suspension are validated according to the real prototype, *Range Rover Evoque*, investigated in the European project *EVE*, (http://eve-project.eu/). All-season 225/55R19 tyres are parameterized accordingly.

In the scenario, the vehicle is assumed to be equipped with the modelled *M*R dampers. The corresponding force-velocity diagrams are shown in Figure 12. The characteristic represented as solid line shows the best parameter fit.

Table 5. Model parameter values obtained using c-FOA, GA and PSO

Parameter No.		Fit 1 (c-FOA) $f(\mathbf{s}) = 3.42 \cdot 10^7$	Fit 2 (GA) $f(\mathbf{s}) = 4.14 \cdot 10^7$	Fit 3 (PSO) $f(\mathbf{s}) = 3.96 \cdot 10^7$
1	m	3.83	21.48	18.79
2	F_0	–275.00	–203.00	–201.00
3	β	144.00	929.00	5926
4	λ	1.41	20.00	0.53
5	F_{ya}	5.56	88.00	30.42
6	F_{yb}	238.00	221.00	235.00
7	C_{ca}^{+}	2278.00	13.00	537.00
8	C_{ca}^{-}	98.00	0.80	816.00
9	C_{cb}^{+}	46.00	834.00	347.00
10	C_{cb}^{-}	178.00	87.00	119.00
11	K_{ka}	3.70	4.64	5.33
12	K_{kb}	1.07	0.43	0.17
13	η	25.00	25.00	25.00

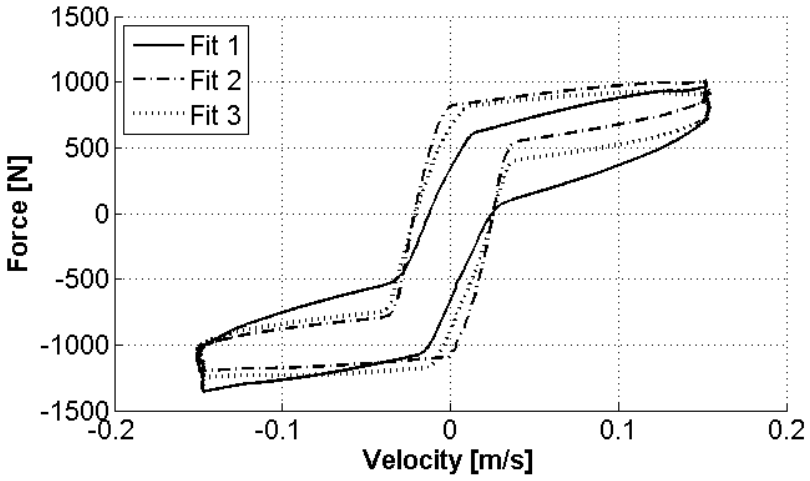

Figure 12. Force-velocity diagrams for three different *MR* damper model parameter sets given in Table 2.

In the scenario an out-of-phase sine-sweep test with variable amplitude is assumed to excite the vehicle. This is a standard test for evaluating ride comfort in the automotive industry. In this test, the peak-to-peak amplitude of the road profile z_r is progressively reduced from 0.004 to 0.001 m and its frequency content increases up to 18 Hz, Figure 13d. This test allows assessing ride comfort characteristics in terms of heave a_{zb}, pitch $\ddot{\theta}_{zb}$ and roll motion $\ddot{\varphi}_{zb}$ in the frequency domain. It is assumed that the vehicle is moving at a constant velocity of 25 m/s. As observed from Figures 13a - 13c the frequency response is not identical between the three parameter fits. In the critical – for ride comfort – frequency range 4-8 Hz the differences are up to 5 dB, while at higher frequencies the discrepancy raises up to 12 dB.

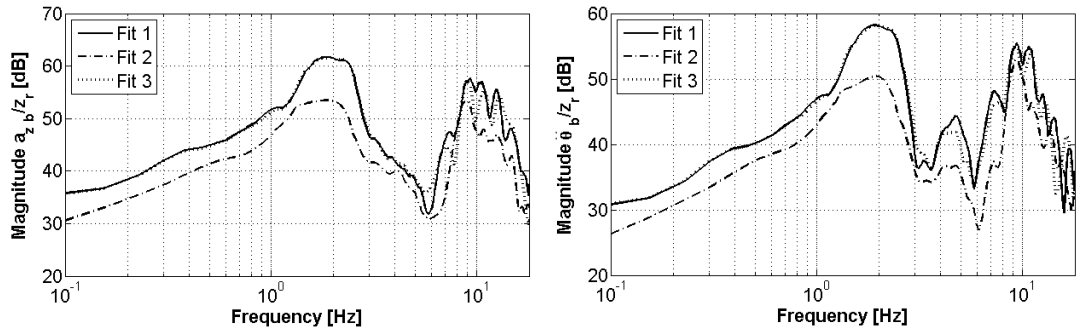

(a) (b)

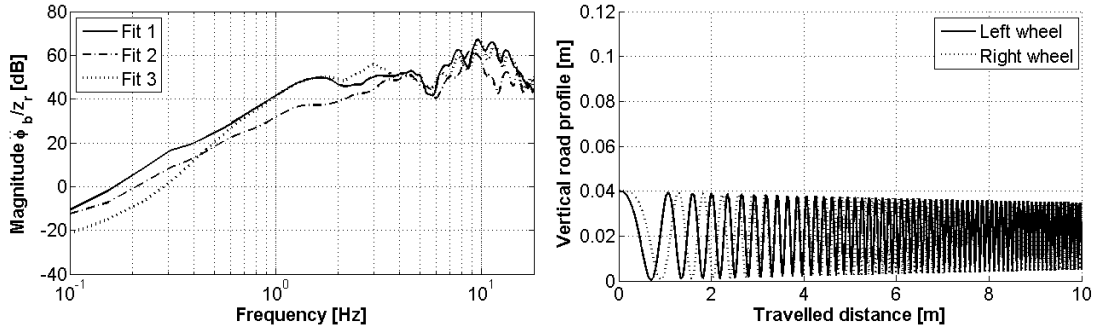

(c) (d)

Figure 13. Simulation results for three different *MR* damper model parameters: (a)

5. c-FOA ANALYSIS

5.1 Parallel computing

c-FOA is a simple Swarm Intelligence algorithm that, with only a few code changes, can be processed in parallel. A computational burden study was conducted on a PC running Windows 7 Enterprise, 64 bit operating system, with an Intel Core i5 processor running at 3.20 GHz and 4 GB installed memory (RAM). The purpose of the study was to compare the simulation time required for c-FOA to complete c iterations ($fun_{evals} = 1000$), with and without parallel processing.

Table 6. Computational cost of the data fit problem using c-FOA: serial implementation; parallel implementation with 2 processors; and parallel implementation with 4 processors for K iterations ($fun_{evals} = 1000$)

Computational burden	Serial computing	Parallel computing with 2 processors	Parallel computing with 4 processors
s	201	154	103

From the results, listed in Table 6, it is evident that with parallel processing the computational burden of c-FOA can be significantly reduced. Specifically, it was reduced by 42% and 62.5% using 2 and 4 parallel processors respectively.

5.2 c-FOA tuning – Sensitivity analysis

c-FOA performance depends on a number of parameters including the number of iterations K, the fruit fly population N and the resolution N_{res}. The parameters $\kappa = 5, M = 0.95$ and $c = 0.9$, were kept constant in this analysis. This is because their

optimum values were easy to determine. For example when the delay parameter κ is too small then the algorithm is not robust against noise. By contrast, if the delay parameter κ is too large then the search strategy is switched not quickly enough and the algorithm becomes much slower. Values $\kappa \in [5,10]$ give robust results, when K is in the range of a few hundred generations. Similarly, M denotes the search range radius. For M=0.95 a significantly large area is explored, considering the inverse-square dependency of the fruit fly position in the *c-FOA* algorithm, Equations (13)-(15). This is also the default value for the standard *FOA*. The contraction parameter c determines how quickly the search radius is reduced (refer to Equation (17)) and therefore is linked to the number of generations K. In the case K is in the range of a few hundreds, then $c = 0.9$ provides a good trade-off between exploration and exploitation. If c is too small the search radius reduces quickly (geometric progression) and might lead c-FOA to premature convergence.

On the other hand, the maximum number of iterations K, the population size N and resolution N_{res} are less intuitive to choose. For this reason three parametric studies were conducted.

In the first parametric study the population size varied: $N = 50, 100$ and 150. The maximum number of iterations and resolution were kept constant, $K = 150$ and $N_{res} = 100$. The results are listed in Table 7. An increase in the population size does not improve considerably the best value but produces better results statistically, as the mean value and standard deviation are reduced.

Table 7. Statistical analysis of the optimisation results obtained by applying *c-FOA* 30 independent times. Best value (*BV*), Mean value (*MV*) and Standard deviation (*SD*) for $= 150$, $N = 50, 100$ and 150, $N_{res} = 100, \kappa = 5, M = 0.95$ and $c = 0.9$

c-FOA	Objective function value $f(\mathbf{s})$		
	BV	*MV*	*SD*
$N = 50$	$3.65 \cdot 10^7$	$5.87 \cdot 10^7$	$3.22 \cdot 10^7$
$N = 100$	$3.60 \cdot 10^7$	$4.96 \cdot 10^7$	$1.35 \cdot 10^7$
$N = 150$	$3.46 \cdot 10^7$	$4.61 \cdot 10^7$	$1.47 \cdot 10^7$

In the second parametric study the maximum number of generations was varied: $K = 150, 200$ and 250. The population size and resolution were kept constant, $N = 50$

and $N_{res} = 100$. The results are listed in Table 8. As observed an increase in the number of iterations does not provide any clear benefit.

Table 8. Statistical analysis of the optimisation results obtained by applying *c-FOA* 30 independent times. Best value (*BV*), Mean value (*MV* and Standard deviation (*SD*) for $K = 150, 200, 250$, $N = 50$, $N_{res} = 100, \kappa = 5, M = 0.95$ and $c = 0.9$

c-FOA	Objective function value $f(\mathbf{s})$		
	BV	*MV*	*SD*
$K = 150$	$3.65 \cdot 10^7$	$5.87 \cdot 10^7$	$3.22 \cdot 10^7$
$K = 200$	$3.46 \cdot 10^7$	$4.94 \cdot 10^7$	$2.17 \cdot 10^7$
$K = 250$	$3.45 \cdot 10^7$	$4.76 \cdot 10^7$	$4.36 \cdot 10^7$

In the third parametric study the resolution varied: $N_{res} = 10, 100$, and 1000. The maximum number of iterations and population size were kept constant $K = 150$ and $N = 50$. The results are listed in Table 9. As observed for a very small resolution the results are significantly worse. For a very large resolution N_{res} the results are slightly worse. A large resolution N_{res} does not allow the algorithm to explore quickly the different combinations of parameters for such a multi-parametric problem.

Table 9. Statistical analysis of the optimisation results obtained by applying *c-FOA* 30 independent times. Best value (*BV*), Mean value (*MV* and Standard deviation (*SD*) for $K = 150$, $N = 50$, $N_{res} = 10$, 100 and 1000, $\kappa = 5, M = 0.95$ and $c = 0.9$

c-FOA	Objective function value $f(\mathbf{s})$		
	BV	*MV*	*SD*
$N_{res} = 10$	$6.33 \cdot 10^7$	$1.99 \cdot 10^8$	$2.01 \cdot 10^8$
$N_{res} = 100$	$3.65 \cdot 10^7$	$5.87 \cdot 10^7$	$3.22 \cdot 10^7$
$N_{res} = 1000$	$3.65 \cdot 10^7$	$7.45 \cdot 10^7$	$6.99 \cdot 10^7$

6. CONCLUSIONS

In this study an automotive magnetorheological (MR) damper with asymmetric viscous damping coefficient in jounce and rebound was studied, modelled and designed. For the parameter identification of the MR damper a new swarm optimisation algorithm, the contrast-based Fruit Fly Optimisation (c-FOA) is proposed. The algorithm was compared to popular optimisation algorithms and the results show the c-FOA is robust and requires minimum tuning. In particular:

- The mechanical behaviour of a prototype automotive magnetorheological (MR) damper was presented. Unique experimental data were generated using a set of sinusoidal and triangular input profiles for different currents. An analysis of the mechanical behaviour was conducted and shown that the MR damper present different viscous behaviour in jounce and rebound.
- A modified algebraic model is proposed for modelling the MR damper. As explained, this is preferred compared to differential equation based MR dampers because in parameter identification several thousand function evaluations may be required. A comparison between a symmetric (original) and asymmetric (proposed) model shows that the latter is potentially more suitable.
- Contrast-based Fruit Fly Optimisation Algorithm (c-FOA) is employed for identifying the damper model parameters. It is the first time that FOA, or a version of it, is used to identify the parameters of a magnetorheological damper. The results confirm the suitability of c-FOA for identifying the parameters of the damper.
- c-FOA is compared to the Genetic Algorithm, Differential Evolution, Particle Swarm Optimisation, Artificial Bee Colony and the original FOA. The comparison is performed on the basis of no *a priori* knowledge of the model parameters' range. The analysis shows that Particle Swarm Optimisation and c-FOA achieve the best performance. Particle Swarm Optimisation achieves a slightly better objective function value, while c-FOA achieves a slightly better average objective function value.
- The computational burden of c-FOA can significantly improve by parallel computing. The analysis showed that by using four processors the computational burden was approximately halved.
- A parametric analysis of c-FOA parameters, in particular the number of iterations $\boldsymbol{K}$, population size $\boldsymbol{N}$ and resolution $\boldsymbol{N_{res}}$ was conducted. The analysis showed that the best results were achieved for $\boldsymbol{K = 200}$, $\boldsymbol{N = 250}$ and $\boldsymbol{N_{res} = 100}$. An increase in resolution did not offer any benefit, nor did an increase in the number of iterations.
- The proposed damper model was implemented on a vehicle model ride comfort Computer Aided Engineering analysis. For this purpose, three

different damper parameter sets were chosen: the optimised parameter fit using c-FOA, the Genetic Algorithm and the Particle Swarm Optimisation. The simulation study quantified how much MR damper model uncertainty influences the metrics used in ride comfort studies.

- For a standard sine sweep test significant differences were observed among the different parameter sets. In the critical – for ride comfort – frequency range 4-8 Hz the differences are limited to up to 5 dB, while at higher frequencies the discrepancy raises up to 12 dB. This result is particularly important for virtual sign-off purposes, currently a trend in automotive industry and which will potentially lead to significant reduction of development time and costs.

In the future, it is foreseen to investigate the hybridisation of c-FOA with local search methods and using the identified *MR* damper models for the development of a distributed predictive suspension control concept.

7. ACKNOWLEDGEMENTS

MEF is grateful for funding from the Lloyd's Register Foundation, a charitable foundation helping to protect life and property by supporting engineering-related education, public engagement and the application of research.

We would like to thank Mr Georgios Chrysakis for developing the MR damper current controller and contributing to the experiments.

8. CONFLICT OF INTEREST

The authors declare that they have no conflict of interest.

9. REFERENCES

[1] Weber, F. Semi-active vibration absorber based on real-time controlled MR damper (2014) Mechanical Systems and Signal Processing, 46 (2), pp. 272-288.

[2] Yang, M.-G., Li, C.-Y., Chen, Z.-Q. A new simple non-linear hysteretic model for MR damper and verification of seismic response reduction experiment (2013) Engineering Structures, 52, pp. 434-445.

[3] Kasprzyk, J., Wyrwał, J., Krauze, P. Automotive MR damper modeling for semi-active vibration control (2014) IEEE/ASME International Conference on Advanced Intelligent Mechatronics, AIM art. no. 6878127, pp. 500-505.

[4] Strecker, Z., Mazůrek, I., Roupec, J., Klapka, M. Influence of MR damper response time on semiactive suspension control efficiency (2015) Meccanica, 50 (8), pp. 1949-1959.

[5] http://www.mckinsey.com/industries/automotive-and-assembly/our-insights/a-road-map-to-the-future-for-the-auto-industry, accessed on 25.06.2017

[6] Lutz, A., Schick, B., Holzmann, H., Kochem, M., Meyer-Tuve, H., Lange, O., Mao, Y. and Tosolin, G. (2017). Simulation methods supporting homologation of Electronic Stability Control in vehicle variants. Vehicle System Dynamics, pp.1-66.].

[7] Londoño, J., Neild, S. and Wagg, D. (2015). Using a damper amplification factor to increase energy dissipation in structures. Engineering Structures, 84, pp.162-171.

[8] Sims, N. (2006). Limit Cycle Behavior of Smart Fluid Dampers Under Closed Loop Control. Journal of Vibration and Acoustics, 128(4), p.413.

[9] Zhang, C., Chen, Z., Wang, L. An investigation on the field strength and loading rate dependences of the hysteretic dynamics of magnetorheological dampers (2014) Mechanics of Time-Dependent Materials, 19 (1), pp. 61-74.

[10] Guan, X.C., Guo, P.F., Ou, J.P. Modeling and analyzing of hysteresis behavior of magneto rheological dampers (2011) Procedia Engineering, 14, pp. 2756-2764.

[11] Strecker, Z., Roupec, J., Mazůrek, I., Klapka, M. Limiting factors of the response time of the magnetorheological damper (2015) International Journal of Applied Electromagnetics and Mechanics, 47 (2), art. no. jae140006, pp. 541-550.

[12] Xu, Z., Jia, D. and Zhang, X. (2012). Performance tests and mathematical model considering magnetic saturation for magnetorheological damper. Journal of Intelligent Material Systems and Structures, 23(12), pp.1331-1349.

[13] Ghaffari, A., Hashemabadi, S.H., Ashtiani, M. A review on the simulation and modeling of magnetorheological fluids (2015) Journal of Intelligent Material Systems and Structures, 26 (8), pp. 881-904.

[14] Ashtiani, M., Hashemabadi, S.H., Ghaffari, A. A review on the magnetorheological fluid preparation and stabilization (2014) Journal of Magnetism and Magnetic Materials, 374, pp. 716-730.

[15] Han, Y.-Y., He, G.-T., Lin, Y.-C., Xu, Z.-Y., Zhu, X.-Q., Liu, Y.-F., Zhao, J., Li, X.-Z. Reviews on the magnetic particles of magnetorheological fluids (2013) Gongneng Cailiao/Journal of Functional Materials, 44 (24), pp. 3513-3519.

[16] Goldasz, J. (2016). Insight into magnetorheological shock absorbers: Springer.

[17] http://repository.tudelft.nl/islandora/object/uuid:d369bfac-4d8a-465c-a194-864bbe87d8e8?collection=research, accessed on 16.01.2017

[18] Çeşmeci, Ş., Engin, T. Modeling and testing of a field-controllable magnetorheological fluid damper (2010) International Journal of Mechanical Sciences, 52 (8), pp. 1036-1046.

[19] Guo, P., Guan, X., Ou, J. Physical modeling and design method of the hysteretic behavior of magnetorheological dampers (2014) Journal of Intelligent Material Systems and Structures, 25 (6), pp. 680-696.

[20] Case, D., Taheri, B., Richer, E. A Lumped-Parameter Model for Adaptive Dynamic MR Damper Control (2015) IEEE/ASME Transactions on Mechatronics, 20 (4), art. no. 6918454, pp. 1689-1696.

[21] Hu, G., Liu, Q., Ding, R. and Li, G. (2017). Vibration control of semi-active suspension system with magnetorheological damper based on hyperbolic tangent model. Advances in Mechanical Engineering, 9(5), p.168781401769458.

[22] Khalid, M., Yusof, R., Joshani, M., Selamat, H., Joshani, M. Nonlinear identification of a magneto-rheological damper based on dynamic neural networks (2014) Computer-Aided Civil and Infrastructure Engineering, 29 (3), pp. 221-233.

[23] Zhang, X., Zhang, X., Zhao, Y., Zhao, J. and Xu, Z. (2017). Experimental and numerical studies on a composite MR damper considering magnetic saturation effect. Engineering Structures, 132, pp.576-585.]

[24] Boada, M.J.L., Calvo, J.A., Boada, B.L., Díaz, V. Modeling of a magnetorheological damper by recursive lazy learning (2011) International Journal of Non-Linear Mechanics, 46 (3), pp. 479-485.

[25] Silveira, M., Pontes, B. and Balthazar, J. Use of nonlinear asymmetrical shock absorber to improve comfort on passenger vehicles (2014) Journal of Sound and Vibration, 333(7), pp.2114-2129.

[26] Silveira, M., Wahi, P. and Fernandes, J. (2016). Effects of asymmetrical damping on a 2 DOF quarter-car model under harmonic excitation. Communications in Nonlinear Science and Numerical Simulation, 43, pp.14-24.

[27] Seifi, A., Hassannejad, R. and Hamed, M. Use of nonlinear asymmetrical shock absorbers in multi-objective optimization of the suspension system in a variety of road excitations (2016) Proceedings of the Institution of Mechanical Engineers, Part K: Journal of Multi-body Dynamics.

[28] Ata, W. and Salem, A. (2017). Semi-active control of tracked vehicle suspension incorporating magnetorheological dampers. Vehicle System Dynamics, pp.1-22.

[29] Charalampakis, A.E., Koumousis, V.K. Identification of Bouc-Wen hysteretic systems by a hybrid evolutionary algorithm (2008) Journal of Sound and Vibration, 314 (3-5), pp. 571-585.Metered, H., Bonello, P., Oyadiji, S.O. The experimental identification of magnetorheological dampers and evaluation of

their controllers (2010) Mechanical Systems and Signal Processing, 24 (4), pp. 976-994.

[30] Fellah Jahromi, A., Bhat, R.B., Xie, W.-F. Frequency dependent Spencer modeling of magnetorheological damper using hybrid optimisation approach (2015) Shock and Vibration, 2015, art. no. 382541.

[31] http://www.ijert.org/view-pdf/12128/experimental-investigation-of-the-effect-of-magneto-rheological-mr-damper-on-a-rotating-unbalance-sdof-system, accessed on 16.05.2016

[32] Ayala, H.V.H., Coelho, L.D.S. Cascaded evolutionary algorithm for nonlinear system identification based on correlation functions and radial basis functions neural networks (2016) Mechanical Systems and Signal Processing, 68-69, pp. 378-393.

[33] R. Storn, "On the usage of differential evolution for function optimization," Proceedings of North American Fuzzy Information Processing, Berkeley, CA, 1996, pp. 519-523.

[34] Hu, T., Harding, S. and Banzhaf, W. (2010). Variable population size and evolution acceleration: a case study with a parallel evolutionary algorithm. Genetic Programming and Evolvable Machines, 11(2), pp.205-225.

[35] Kwok, N.M., Ha, Q.P., Nguyen, M.T., Li, J., Samali, B. Bouc-Wen model parameter identification for a MR fluid damper using computationally efficient GA (2007) ISA Transactions, 46 (2), pp. 167-179.

[36] Talatahari, S., Rahbari, N.M. Enriched Imperialist Competitive Algorithm for system identification of magneto-rheological dampers (2015) Mechanical Systems and Signal Processing, 62, pp. 506-516.

[37] Talatahari, S., Kaveh, A., Mohajer Rahbari, N. Parameter identification of Bouc-Wen model for MR fluid dampers using adaptive charged system search optimization (2012) Journal of Mechanical Science and Technology, 26 (8), pp. 2523-2534.

[38] Kwok, N.M., Ha, Q.P., Nguyen, T.H., Li, J., Samali, B. A novel hysteretic model for magnetorheological fluid dampers and parameter identification using particle swarm optimization (2006) Sensors and Actuators, A: Physical, 132 (2), pp. 441-451.

[39] Wang, D.H., Liao, W.H. Magnetorheological fluid dampers: A review of parametric modelling (2011) Smart Materials and Structures, 20 (2), art. no. 023001.

[40] Kanarachos, S., Griffin, J. and Fitzpatrick, M. (2017). Efficient truss optimization using the contrast-based fruit fly optimization algorithm. Computers & Structures, 182, pp.137-148.

[41] Dixon, J. The shock absorber handbook (2008) John Wiley & Sons.

[42] Zhang, J., Yue, J., Zhang, L., Jia, J. and Peng, Z. (2013). Design of Magnetorheological Damper Control System for Vehicle Suspension. Applied Mechanics and Materials, 278-280, pp.1436-1441.

[43] Isermann, R. and Munchhof, M. (2011). Identification of dynamical systems. 1st ed. Berlin: Springer.

[44] Pan, W.-T. A new Fruit Fly Optimisation Algorithm: Taking the financial distress model as an example (2012) Knowledge-Based Systems, 26, pp. 69-74.

[45] Jun-qing Li, Quan-ke Pan, Kun Mao, P.N. Suganthan, Solving the steelmaking casting problem using an effective fruit fly optimisation algorithm, Knowledge-Based Systems, Volume 72, December 2014, Pages 28-36.

[46] Lianghong Wu, Cili Zuo, Hongqiang Zhang, A cloud model based fruit fly optimisation algorithm, Knowledge-Based Systems, Volume 89, November 2015, Pages 603-617.

[47] Marko Mitic, Najdan Vukovic, Milica Petrovic, Zoran Miljkovic, Chaotic fruit fly optimisation algorithm, Knowledge-Based Systems, Volume 89, November 2015, Pages 446-458.

[48] Van Breugel, F., Dickinson, M.H. Plume-tracking behavior of flying drosophila emerges from a set of distinct sensory-motor reflexes (2014) Current Biology, 24 (3), pp. 274-286.

[49] http://www.nncn.de/en/news/Forschungsergebnisse-en/memories-of-fruit-fly-larvae-are-more-complex-than-thought, accessed on 17.12.2016.

[50] Alajmi, A. and Wright, J. (2014). Selecting the most efficient genetic algorithm sets in solving unconstrained building optimization problem. International Journal of Sustainable Built Environment, 3(1), pp.18-26.

[51] http://www1.icsi.berkeley.edu/~storn/code.html, accessed on 17.12.2016.

[52] https://pdfs.semanticscholar.org/48aa/36e1496c56904f9f6dfc15323e0c45e34a4c.pdf, accessed on 17.12.2016.

[53] Shi Y., Eberhart R.C. (1998) Parameter selection in particle swarm optimization. In: Porto V.W., Saravanan N., Waagen D., Eiben A.E. (eds) Evolutionary Programming VII. EP 1998. Lecture Notes in Computer Science, vol 1447. Springer, Berlin, Heidelberg

[54] Diwold, K., Aderhold, A., Scheidler, A. and Middendorf, M. (2011). Performance evaluation of artificial bee colony optimization and new selection schemes. Memetic Computing, 3(3), pp.149-162

[55] http://www1.icsi.berkeley.edu/~storn/code.html#matl, accessed on 16.01.2017

[56] L. Guoqiang, P. Niu, and X. Xiao. Development and Investigation of Efficient Artificial Bee Colony Algorithm for Numerical Function Optimization, Applied Soft Computing, vol. 12, no. 1, pp. 320-332, 2012.

[57] https://www.mathworks.com/matlabcentral/answers/uploaded_files/20100/Fruit%20Fly%20Optimization%20Algorithm_Second%20Edition.pdf, accessed on 17.12.2016.

[58] Savitski, D., Ivanov, V., Augsburg, K., Dhaens, M., Els, S., Sandu, C. State-Of-The-Art and Future Developments in Integrated Chassis Control for Ground Vehicl

Appendix A

Table 10. Statistical analysis of the optimisation results obtained by applying Genetic Algorithm, 30 independent times. BV: Best value, MV: Mean value, SD: Standard deviation

Genetic Algorithm	Objective function value $f(\mathbf{s})$		
	BV	*MV*	*SD*
N=50, fun_evals=4000	$1.25 \cdot 10^{8}$	$8.35 \cdot 10^{8}$	$1.02 \cdot 10^{9}$
N=50, fun_evals=8000	$4.62 \cdot 10^{7}$	$3.12 \cdot 10^{8}$	$7.50 \cdot 10^{8}$
N=50, fun_evals=16000	$3.70 \cdot 10^{7}$	$9.98 \cdot 10^{7}$	$3.20 \cdot 10^{8}$
N=100, fun_evals=4000	$2.98 \cdot 10^{8}$	$1.39 \cdot 10^{9}$	$5.88 \cdot 10^{8}$
N=100, fun_evals=8000	$6.12 \cdot 10^{7}$	$2.95 \cdot 10^{8}$	$6.92 \cdot 10^{8}$
N=100, fun_evals=16000	$4.14 \cdot 10^{7}$	$4.67 \cdot 10^{7}$	$3.11 \cdot 10^{6}$
N=150, fun_evals=4000	$1.20 \cdot 10^{9}$	$2.67 \cdot 10^{11}$	$1.45 \cdot 10^{12}$
N=150, fun_evals=8000	$6.78 \cdot 10^{7}$	$3.89 \cdot 10^{8}$	$2.42 \cdot 10^{8}$
N=150, fun_evals=16000	$4.40 \cdot 10^{7}$	$1.35 \cdot 10^{8}$	$4.63 \cdot 10^{8}$

Table 11. Statistical analysis of the optimisation results obtained by applying Differential Evolution, 30 independent times. BV: Best value, MV: Mean value, SD: Standard deviation

Differential Evolution	Objective function value $f(\mathbf{s})$		
	BV	*MV*	*SD*
N=50, fun_evals=4000	$1.97 \cdot 10^{10}$	$4.18 \cdot 10^{10}$	$1.42 \cdot 10^{10}$
N=50, fun_evals=8000	$3.97 \cdot 10^{9}$	$7.61 \cdot 10^{9}$	$3.83 \cdot 10^{9}$

N=50, fun_evals=16000	$3.76 \cdot 10^{8}$	$9.31 \cdot 10^{8}$	$4.66 \cdot 10^{8}$
N=100, fun_evals=4000	$5.52 \cdot 10^{10}$	$1.28 \cdot 10^{11}$	$4.83 \cdot 10^{10}$
N=100, fun_evals=8000	$1.45 \cdot 10^{10}$	$4.16 \cdot 10^{10}$	$1.5 \cdot 10^{10}$
N=100, fun_evals=16000	$2.64 \cdot 10^{9}$	$7.28 \cdot 10^{9}$	$2.25 \cdot 10^{9}$
N=150, fun_evals=4000	$7.72 \cdot 10^{10}$	$1.98 \cdot 10^{11}$	$6.95 \cdot 10^{10}$
N=150, fun_evals=8000	$1.58 \cdot 10^{10}$	$6.86 \cdot 10^{10}$	$2.12 \cdot 10^{10}$
N=150, fun_evals=16000	$8.85 \cdot 10^{9}$	$2.18 \cdot 10^{10}$	$7.54 \cdot 10^{9}$

Table 12. Statistical analysis of the optimisation results obtained by applying, 30 independent times, Particle Swarm Optimization. BV: Best value, MV: Mean value, SD: Standard deviation

Particle Swarm Optimization	Objective function value $f(\mathbf{s})$		
	BV	*MV*	*SD*
N=50, fun_evals=4000	$3.83 \cdot 10^{7}$	$1.53 \cdot 10^{8}$	$9.80 \cdot 10^{7}$
N=50, fun_evals=8000	$3.46 \cdot 10^{7}$	$6.94 \cdot 10^{7}$	$2.68 \cdot 10^{7}$
N=50, fun_evals=16000	$3.39 \cdot 10^{7}$	$5.57 \cdot 10^{7}$	$1.05 \cdot 10^{7}$
N=100, fun_evals=4000	$4.12 \cdot 10^{7}$	$4.92 \cdot 10^{8}$	$5.45 \cdot 10^{8}$
N=100, fun_evals=8000	$3.45 \cdot 10^{7}$	$8.59 \cdot 10^{7}$	$4.88 \cdot 10^{7}$
N=100, fun_evals=16000	$3.39 \cdot 10^{7}$	$5.44 \cdot 10^{7}$	$1.40 \cdot 10^{7}$
N=150, fun_evals=4000	$1.19 \cdot 10^{8}$	$9.35 \cdot 10^{9}$	$1.12 \cdot 10^{9}$
N=150, fun_evals=8000	$4.14 \cdot 10^{7}$	$1.42 \cdot 10^{8}$	$1.32 \cdot 10^{8}$
N=150, fun_evals=16000	$3.36 \cdot 10^{7}$	$5.87 \cdot 10^{7}$	$1.63 \cdot 10^{7}$

Table 13. Statistical analysis of the optimisation results obtained by applying, 30 independent times, Artificial Bee Colony. BV: Best value, MV: Mean value, SD: Standard deviation

Artificial Bee Colony	Objective function value $f(\mathbf{s})$		
	BV	*MV*	*SD*

N=50, fun_evals=4000	$2.58 \cdot 10^{10}$	$6.39 \cdot 10^{10}$	$2.25 \cdot 10^{10}$
N=50, fun_evals=8000	$5.89 \cdot 10^{9}$	$2.80 \cdot 10^{10}$	$1.12 \cdot 10^{10}$
N=50, fun_evals=16000	$2.96 \cdot 10^{9}$	$1.14 \cdot 10^{10}$	$6.39 \cdot 10^{9}$
N=100, fun_evals=4000	$4.12 \cdot 10^{10}$	$1.08 \cdot 10^{11}$	$4.13 \cdot 10^{10}$
N=100, fun_evals=8000	$1.85 \cdot 10^{10}$	$5.15 \cdot 10^{10}$	$1.96 \cdot 10^{10}$
N=100, fun_evals=16000	$9.35 \cdot 10^{9}$	$2.29 \cdot 10^{10}$	$1.16 \cdot 10^{10}$
N=150, fun_evals=4000	$4.64 \cdot 10^{10}$	$1.2 \cdot 10^{11}$	$5.36 \cdot 10^{10}$
N=150, fun_evals=8000	$2.15 \cdot 10^{10}$	$5.63 \cdot 10^{10}$	$2.82 \cdot 10^{10}$
N=150, fun_evals=16000	$8.55 \cdot 10^{9}$	$3.45 \cdot 10^{10}$	$1.40 \cdot 10^{10}$

Table 14. Statistical analysis of the optimisation results obtained by applying, 30 independent times, c-FOA. BV: Best value, MV: Mean value, SD: Standard deviation

c-FOA	Objective function value $f(\mathbf{s})$		
	BV	*MV*	*SD*
N=50, fun_evals=4000	$4.14 \cdot 10^{7}$	$1.43 \cdot 10^{8}$	$1.\ 38 \cdot 10^{8}$
N=50, fun_evals=8000	$3.65 \cdot 10^{7}$	$5.72 \cdot 10^{7}$	$4.35 \cdot 10^{7}$
N=50, fun_evals=16000	$3.40 \cdot 10^{7}$	$4.53 \cdot 10^{7}$	$1.44 \cdot 10^{7}$
N=100, fun_evals=4000	$8.29 \cdot 10^{8}$	$3.21 \cdot 10^{15}$	$9.24 \cdot 10^{15}$
N=100, fun_evals=8000	$3.81 \cdot 10^{7}$	$1.04 \cdot 10^{8}$	$1.34 \cdot 10^{8}$
N=100, fun_evals=16000	$3.64 \cdot 10^{7}$	$6.70 \cdot 10^{7}$	$6.02 \cdot 10^{7}$
N=150, fun_evals=4000	$2.00 \cdot 10^{17}$	$2.00 \cdot 10^{17}$	$3.34 \cdot 10^{12}$
N=150, fun_evals=8000	$5.21 \cdot 10^{7}$	$2.37 \cdot 10^{8}$	$2.37 \cdot 10^{8}$
N=150, fun_evals=16000	$3.54 \cdot 10^{7}$	$5.66 \cdot 10^{7}$	$1.85 \cdot 10^{7}$